Macromolecules **2000,** *33,* 3031−3041

An Attempt To Separate Roughness from Interdiffusion in the Interfacial Broadening between Two Immiscible Polymers

V. W. Stone,[†] X. Arys, R. Legras, and A. M. Jonas*

Unité de Chimie et de Physique des Hauts Polymères, Université catholique de Louvain, 1, Place Croix du Sud, B-1348 Louvain-la-Neuve, Belgium

Received March 1, 1999; Revised Manuscript Received February 4, 2000

ABSTRACT: A detailed study of the interface formation between polystyrene (PS) and chlorinated polybutadiene (CPB) at 150 °C is carried out on bilayer samples by X-ray reflectometry (XRR) and X-ray diffuse scattering (XDS). An equilibrium melt interfacial width $\sigma_m(150\ °C) = 18.8 \pm 0.3$ Å is determined by XRR. Lateral fluctuations being averaged over the coherence area in this method, σ_m must be considered as originating from both homopolymer interdiffusion ($\sigma_{CPB/PS}$) and interfacial roughness (σ_r): $\sigma_m^2 = \sigma_{CPB/PS}^2 + \sigma_r^2$. Interfacial roughness is generally described in the literature to be due to either a residual roughness from sample preparation (hypothesis 1) or capillary fluctuations building up at the interface (hypothesis 2). The nature and importance of the interfacial roughness are assessed by XDS scans, which include the detection of the diffuse (off-specular) scattering arising from lateral correlations in the roughness profile. While hypothesis 1 can be unambiguously rejected from the analysis of our XDS data, at least two equally valuable fits of theory to data are found under the hypothesis that the interfacial roughness changes during annealing. In the first one, interdiffusion is restricted, and the interfacial width is dominated by roughness ($\sigma_r > \sigma_{CPB/PS}$). In the second one, the reverse is true: $\sigma_{CPB/PS} \gg \sigma_r$. The former picture is closer to predictions from existing molecular theories of capillarity and gives for the Flory−Huggins interaction parameter computed through mean-field arguments a better agreement with the interaction parameter obtained from solubility parameters of CPB and PS.

Introduction

Because of the increasingly large number of applications involving interfaces between polymeric species (coextrusion, immiscible blends, etc.), many efforts have been made during this past decade to experimentally characterize the structure and composition profile of the interface between two homopolymers A and B. Depending on the miscibility between A and B, depth profiling techniques with appropriate depth resolutions have been used (e.g., dynamic secondary ion mass spectroscopy,[2] forward recoil spectroscopy,[2,3] nuclear reaction analysis[4,5]). For immiscible homopolymers with typical interfacial widths of 20−100 Å, the angstrom resolution of the specular reflectivity techniques is generally required.[6] Neutron reflectometry (NR) has already been applied to a few immiscible systems where deuteration was used to generate large contrasts[6] (*d*-PS/poly(methyl methacrylate),[7−9] *d*-PS/poly(*n*-butyl methacrylate),[10,11] *d*-PS/polyethylene[12]). As deuteration may be a perturbing factor for real polymer systems, X-ray reflectometry (XRR) would appear at first sight better suited to such studies. However, due to much smaller contrasts, examples of studies using XRR (PS/poly(*p*-bromostyrene)[13]) are scarcer.

Thanks to mean field theories predicting the interfacial thickness in terms of the Flory−Huggins χ_{AB} parameter,[14,15] these reflectometry techniques have often been considered as a method of choice to evaluate χ_{AB} for immiscible A/B blends. Indeed, owing to the drawbacks of the other methods measuring osmotic pressure,[16] gas sorption via inverse gas chromatography,[17] melting point depressions,[18] heat of mixing,[19] light scattering,[20] cloud points,[21,22] solubility parameters,[23] and small-angle X-ray[24] or neutron[25,26] scattering, the range of values reported for a given A−B segment pair is in general so large that no reliable miscibility behavior can be deduced. Using Gaussian random walk statistics and resolving the Edwards self-consistent fields equations, Helfand and co-workers[14,15] predicted a $\chi_{AB}^{-1/2}$ dependence for the interfacial width σ_{AB}^{∞} in incompressible blends of homopolymers with infinite chain length (P_A, $P_B \rightarrow \infty$) in the strong segregation limit ($\chi_{AB}P_A$, $\chi_{AB}P_B \gg 1$):

$$\sigma_{AB}^{\infty} = \frac{2}{\sqrt{2\pi}}\left(\frac{b_A^2/v_A + b_B^2/v_B}{12\chi_{AB}/(v_A v_B)^{1/2}}\right) \qquad (1)$$

where b_A and b_B are the statistical segment lengths of the two components with monomer specific volumes v_A and v_B, respectively. The factor $1/\sqrt{2\pi}$ not present in the Helfand's theory converts the hyperbolic tangent width originally used to define the interfacial width to the standard deviation of an error profile which will be the definition of the interfacial width in use in this study.[8]

As already pointed out by many authors,[6,8−13] equilibrium interfacial widths measured by specular reflectometry (σ_m) are systematically ca. 70% in excess of the values calculated taking only interdiffusion into account (eq 1). The origins of this discrepancy are however still unclear. A first factor to be considered is the finite length of the chains. As the shorter the chains the more severe the loss of entropy due to confinement of the chains into one-half space, the interface should be broader for small chains.[27] For homopolymers of degree of polymerization P_A and P_B, this effect has been described by

$$\sigma_{AB} = \sigma_{AB}^{\infty}\left(1 - 2L\left(\frac{1}{\chi_{AB}P_A} + \frac{1}{\chi_{AB}P_B}\right)\right)^{-1/2} \qquad (2)$$

[†] Current address: UCB Chemicals s.a., Research and Technology, 33 rue d'Anderlecht, B-1620 Drogenbos, Belgium.

10.1021/ma990306u CCC: $19.00

where $L = \ln 2$[27] or $^5/_8$[28] depending on the theoretical approach. In practice, the finite chain length effect is small for homopolymers;[29] the induced broadening, typically amounting to a few percent, cannot alone explain the above-mentioned discrepancy.

Some authors[6,10,11,13] accounted the remaining difference to the residual roughness σ_0 induced by the sample preparation before annealing. They assumed that these fluctuations remain constant throughout the annealing treatment and add in quadrature to the intrinsic interfacial width σ_{AB}:

$$\sigma_m^2(T) = \sigma_{AB}^2(T) + \sigma_0^2 \quad (3)$$

Arguing that, if annealed long enough, the interface should attain an equilibrium independent of the starting state of the system, other authors[8,29−31] claimed that the mean-field or intrinsic interface of width σ_{AB} is roughened by thermally excited capillary waves:

$$\sigma_m^2(T) = \sigma_{AB}^2(T) + \sigma_{fl}^2(T) \quad (4)$$

Despite uncertainties in the expression for the interfacial mean-square displacement $\sigma_{fl}^2(T)$ due to capillary waves, experimental evidence for the presence of these fluctuations has recently been given.[9]

From the above discussion, a stringent need for direct experimental observation of the evolution of the roughness profile at the A/B interface upon annealing clearly appears. In this paper, XRR has been used to study the interface formation between PS and chlorinated polybutadiene (CPB) at 150 °C. As XRR experiments are sensitive to laterally averaged electron density fluctuations along the sample normal only,[32] concomitant X-ray diffuse scattering (XDS) measurements have been performed to bring information on electron density correlations in the plane of the CPB/PS interface. As explained in the next section, these correlations are directly related to the existence of roughness at the interface and may help to select between eq 3 and eq 4.

Roughness and X-ray Diffuse Scattering

In this section, we review briefly the main aspects of X-ray diffuse scattering (XDS) as applied to the characterization of rough surfaces and multilayers. Theories describing XDS by multilayers have been published in recent years within the frame of the distorted wave Born approximation (DWBA), allowing to compute the diffuse scattering even at the vicinity of the critical angle for total external reflection.[33−35] For a multilayer in which the N interfaces are sufficiently spaced apart to eliminate cross-correlations between their roughness profiles, the differential scattering cross section for the diffuse (or incoherent) scattering reads

$$\frac{d\sigma_{\text{diffuse}}}{d\Omega}(q_x,q_y) = \sum_{j=1}^{N} \frac{d\sigma_{j,\text{diffuse}}}{d\Omega}(q_x,q_y) \quad (5)$$

with

$$\frac{d\sigma_{j,\text{diffuse}}}{d\Omega}(q_x,q_y) \propto \sum_{\nu,\nu'=1}^{4} e^{-0.5\sigma_j{}^2(q_{j,\nu}^2+q_{j,\nu'}^{*2})} \int dx\, dy \times [e^{q_{j,\nu}q_{j,\nu'}^{*}C_{jj}(R)} - 1]e^{-i(q_x x+q_y y)} \quad (6)$$

where $R = (x^2 + y^2)^{1/2}$, q_x and q_y are the components (in air) of the scattering vector in the plane of the multilayer (x,y-plane), and the $q_{j,\nu}$'s are defined in ref 34. The proportionality factor, which is not written here, is a complicated function of refraction indexes, scattering vector lengths, and X-ray wavelength; it can be found in ref 34. Of importance here is the fact that the contribution of each interface j to the diffuse scattering depends on the rms roughness σ_j of this interface (which describes the average vertical extent of the height fluctuation of interface j) and on the height−height correlation function $C_{jj}(R)$ of interface j (which describes the lateral evolution of roughness). The correlation function is defined as

$$C_{jj}(R{=}|\mathbf{R}|) = \langle u_j(\mathbf{r})\cdot u_j(\mathbf{r}-\mathbf{R})\rangle \quad (7)$$

where u_j is the local height deviation of interface j from its average height, and $\langle f\rangle$ means the average of f over the (x,y) plane. With this definition, $\sigma_j^2 = C_{jj}(0)$.

For an interface sustaining a spectrum of thermally excited capillary waves, one may write[36−38]

$$C_{jj}(R) = \frac{kT}{2\pi\gamma}\left[K_0\left(R\sqrt{\frac{\Delta\rho g + \alpha}{\gamma}}\right) - K_0\left(R\sqrt{\frac{\gamma}{K}}\right)\right] \quad (8)$$

where γ is the macroscopic interfacial tension of interface j, $\Delta\rho$ is the mass density difference across interface j, and K is the bending rigidity of that interface which, for the simplest case, equals $^3/_8\pi kT$ due to mode coupling.[37] The constant α is a term taking into account long-range forces (except gravity) which affect the spectrum of capillary waves. For instance, for a thin film deposited on a substrate, the spectrum of capillary waves at the film free surface will depend on the van der Waals interaction[39] across the thin film. In this case, $\alpha = A/(2\pi D^4)$, where D is the film thickness and A is the Hamaker constant for the interaction between substrate and air through the film.[9,40]

Equation 8 is only valid for the special case of a roughness due to capillary waves. For many real solid interfaces, the following expression has been proposed[41] for $C_{jj}(R)$:

$$C_{jj}(R) = \sigma_j^2 e^{-(R/\xi_j)^{2H_j}} \quad (9)$$

with ξ_j the in-plane correlation length and H_j the so-called Hurst exponent. This expression is strictly valid only for self-affine surfaces. However, this expression is of more general applicability. It can indeed be verified that, for reasonable values of $\Delta\rho$, α, and γ, expression 9 can be fitted to eq 8 through the proper choice of ξ and H, which means that eq 9 is intrinsically also able to represent a spectrum of capillary waves. In the present paper we will thus consistently use eq 9 to fit the XDS, thereby not restricting ourselves a priori to roughness due to capillary fluctuations.

A final point to note is that eq 8 was derived without introducing cutoffs for the long and short wavelengths that can be sustained by the interface, as is usually done.[42−46] The circular Fourier transform of $C_{jj}(R)$ in eq 8, which is called the power spectral density of capillary waves, reads

$$P_{jj}(s) = 2\pi\int_0^\infty RC_{jj}(R)J_0(2\pi sR)\, dR = \frac{kT}{\Delta\rho g + \alpha + \gamma(2\pi s)^2 + K(2\pi s)^4} \quad (10)$$

From this expression, one can easily obtain through the use of Parseval's theorem the roughness that would be measured in an ideal experiment (perfect collimation):

$$\sigma_{j,\mathrm{ideal}}^2 = \int_0^\infty 2\pi s P_{jj}(s)\,\mathrm{d}s \cong \frac{kT}{2\pi\gamma}\ln\left(\frac{q_\mathrm{U}}{q_{\mathrm{L,ideal}}}\right) \qquad (11)$$

with $q_\mathrm{U} = (\gamma/K)^{1/2}$ and $q_{\mathrm{L,ideal}} = ((\Delta\rho g + \alpha)/\gamma)^{1/2}$. However, for any real experiment, eq 5 must be convolved by experimental resolution functions, which is similar to introducing a long wavelength cutoff in the power spectrum of capillary waves.[41] This is because X-rays effectively probe the roughness over a length scale equal to their coherence length projected in the plane of the multilayer (L_cx). Hence, they cannot "feel" capillary waves of wavelength larger than L_cx, which implies that the roughness as obtained from a real scattering experiment must be written as

$$\sigma_j^2 = \int_{1/L_\mathrm{cx}}^\infty 2\pi s P_{jj}(s)\,\mathrm{d}s \cong \frac{kT}{2\pi\gamma}\ln\left(\frac{q_\mathrm{U}}{q_\mathrm{L}}\right) \qquad (12)$$

with $q_\mathrm{L} = (q_{\mathrm{L,ideal}}^2 + q_{\min}^2)^{1/2}$ and $q_{\min} = 2\pi/L_\mathrm{cx}$. In this work, all theoretical expressions for the XDS were convolved by experimental resolution functions, which ensures that roughness waves of wavelength longer than the coherence length of the photons are effectively excluded from the XDS.

Experimental Section

Materials. Homodisperse CPB was obtained from the chlorination in solution of a homodisperse polybutadiene. The absolute number-average molecular weight ($\bar{M}_{\mathrm{n,CPB}} = 33\,600$) and polydispersity index ($\bar{M}_{\mathrm{w,CPB}}/\bar{M}_{\mathrm{n,CPB}} = 1.04$) were determined as reported elsewhere.[47] Elemental analysis and size exclusion chromatography both showed that about 85% of the double bonds originally present were chlorinated. The T_g of CPB was found equal to 61 °C by differential scanning calorimetry.[47]

A homodisperse anionic H-terminated PS with similar average weight and polydispersity index ($\bar{M}_{\mathrm{n,PS}} = 46\,000$ and $\bar{M}_{\mathrm{w,PS}}/\bar{M}_{\mathrm{n,PS}} < 1.05$) was obtained from Waters. $T_\mathrm{g} = 101$ °C as determined by differential scanning calorimetry.[47]

Sample Preparation. CPB/PS bilayers with PS at the top were prepared by using conventional deposition methods.[6] PS and CPB were first dissolved in distilled toluene and deposited by spin-coating (acceleration: 20 000 rpm/s) onto a 5 × 5 cm^2 float glass substrate and a 1.5 × 1.5 cm^2 square cut from 2 in. diameter silicon wafers (n-type, ⟨100⟩ orientation from Wäcker), respectively. Concentrations ranging from 1 to 3% (w/v) and rotation speeds from 2000 to 4000 rpm were used depending on the desired thickness. Before the formation of the bilayer, the electron density profiles of the single films systems were determined by XRR.

Subsequently, the sides of the glass substrate were scored with a razor blade, and the PS film was floated off onto a pool of Milli-Q water and picked up by a CPB film still deposited on a silicon substrate. Before polymer deposition, the silicon substrates were thoroughly cleaned in a pirhana solution (1:2 (v/v) H_2SO_4 98%/H_2O_2 30 wt % mixture) at 80 °C for 20 min to remove organic contaminants while leaving a 10−20 Å thick SiO_x layer.[48] By contrast, the glass surfaces were only gently wiped out with a tissue previously soaked in 2-propanol. The bilayer system was then dried for 24 h under vacuum at 40 °C.

Samples were characterized by X-ray reflectometry and X-ray diffuse scattering before and after being annealed at 150 °C, 49 °C above the highest bulk T_g of both components. The sample annealing was performed under vacuum for lengths of time varying up to 24 h and was followed by quenching the sample in air. The absence of film dewetting was checked by optical microscopy before performing any X-ray experiment.

X-ray Reflectometry and X-ray Diffuse Scattering. The coherently (specular) and incoherently (diffuse) scattered intensities were recorded with a $\theta-\theta$ goniometer whose geometry is described elsewhere.[49] In X-ray reflectometry (XRR) scans, the incident angle θ_1^0 and the exit angle θ_2^0 are kept equal to θ^0. The coherent scattered intensities are detected along the *z*-component of the incident wave vector $k_{1z} = 2\pi/\bar{\lambda}\,\sin\,\theta_1^0$. In X-ray diffuse scattering (XDS), the diffuse component of the scattering is observed in a wide angular range around the specularly reflected beam through rocking scans. The sum $\theta_1^0 + \theta_2^0$ is kept at a constant value θ_m^0 which is the central angle around which the scan is performed. For low θ_m^0, this amounts to probing the scattered intensity along the *x*-component of the wave vector transfer $q_x = 2\pi/\bar{\lambda}\cdot(\cos\,\theta_1^0 - \cos\,\theta_2^0)$, the perpendicular component q_z remaining almost constant.

XRR data were corrected for spillover effects.[49] Electron density profiles were obtained using a delumping procedure minimizing preliminary assumptions concerning their shape.[49] Basically, these profiles were first approximated by a succession of *M* slabs of uniform density ρ_i ($1 \le i \le M$, $i = 0$ is the substrate). From this model, the reflectivity can be computed by Parrat's method;[50] the thickness and density of each slab were then optimized in order to minimize

$$\chi_{\mathrm{XRR}}^2 = \sum_{j=1}^{N}\left(\frac{R_{\mathrm{meas},j} - R_{\mathrm{calc},j}}{w_j}\right)^2 + \lambda\sum_{i=0}^{M-1}(\rho_{i+1} - \rho_i)^2 \qquad (13)$$

In eq 13, the first term is a weighted sum of residuals obtained from the *N* measured reflectivities $R_{\mathrm{meas},j}$ and corresponding reflectivities calculated from the model density profile, while the second term is a regularizing term introduced to avoid spurious oscillations in the electron density profiles.[51] The standard error on each point *j* was taken as weight (w_j), except in the first stages of the fit where empirically determined weights were used to favor convergence.[49] The whole fitting process was repeated with increasing number of slabs until each slab was sufficiently thin not to introduce artificial oscillations in the computed reflectivity over the experimental angular range.[32] From this discrete profile, a continuous profile was computed, consisting in a superposition of 2−3 virtual layers each with its own thickness d_i, density ρ_i, and interfacial widths σ_i. The final fit was performed with this simplified model. Calculated reflectivities were convolved by a Gaussian resolution function estimated from the divergence of the beam and the wavelength distribution.[49]

The coherent intensity detected *in rocking scans* can be written

$$\tilde{N}_{\mathrm{spec}}(\theta_1^0,\theta_2^0) = K\tilde{N}_{0,\mathrm{spec}}T_{\mathrm{spec}}(|\mathbf{r}|^2,\theta_1^0,\theta_2^0) \qquad (14)$$

K being a scaling factor, $\tilde{N}_{0,\mathrm{spec}}$ the flux of incident photons, and $T_{\mathrm{spec}}(|\mathbf{r}|^2,\theta_1^0,\theta_2^0)$ the transmittance of the specular scattering depending on the reflectivity $|r|^2$ and the geometry of the system.[49] The unconvolved incoherent (diffuse) intensity is given by[49]

$$\tilde{N}_{\mathrm{diffuse}}(\theta_1^0,\theta_2^0) = K\tilde{N}_{0,\mathrm{diffuse}}(\theta_1^0,\theta_2^0)/A_0(\theta_1^0,\theta_2^0)\frac{\mathrm{d}\sigma_{\mathrm{diffuse}}}{\mathrm{d}\Omega}(\theta_1^0,\theta_2^0)\Delta\Omega \qquad (15)$$

$\tilde{N}_{0,\mathrm{diffuse}}(\theta_1^0,\theta_2^0)$ is the flux of incident photons which can be "seen" by the sample and detected during a rocking scan. It has been computed in ref 49 and is equal to $\tilde{N}_{0,\mathrm{spec}}$ at specular position. $A_0(\theta_1^0,\theta_2^0) \sim \sin\,\theta_1^0$ is the efficient cross section of the beam at the sample and has been computed in ref 49 for our experimental geometry. $\Delta\Omega$ is the solid angle subtended by the detector slit. Convolved incoherent intensities $\tilde{N}_{\mathrm{diffuse}}^{\mathrm{conv}}$ were obtained by use of resolution functions which are, unlike in XRR scans, different for incident and scattered rays and dependent on the angular position of the source θ_1^0 and detector θ_2^0.[49] The electron density profile perpendicular to the sample surface once derived from XRR, XDS data gave access to electron density correlations in the sample plane as detailed in a previous section. Similarly to the analysis of XRR data, the correlation lengths and roughness parameters were adjusted by minimizing with the aid of the Levenberg–Marquardt method the weighted sum of residuals:

$$\chi^2_{\mathrm{XDS}} = \sum_{j=1}^{N'} \left(\frac{(\tilde{N}/\tilde{N}_{0,\mathrm{spec}})_{\mathrm{meas},j} - (\tilde{N}/\tilde{N}_{0,\mathrm{spec}})_{\mathrm{calc},j}}{s_j} \right)^2 \qquad (16)$$

where $\tilde{N} = \tilde{N}_{\mathrm{spec}} + \tilde{N}^{\mathrm{conv}}_{\mathrm{diffuse}}$ and s_j is, as above, the standard error on the N' measured intensities. The calculated intensities $(\tilde{N}/\tilde{N}_{0,\mathrm{spec}})_{\mathrm{calc},j}$ were obtained using for the differential cross section for diffuse scattering appearing in eq 15, the general expression derived for rough multilayers within the distorted wave Born approximation up to first order (DWBA). In-depth presentation and discussion on the limits of this theory may be found in refs 34, 49, and 52. Reliable parameters have been obtained by fitting simultaneously a few rocking curves spanning large portions of the reciprocal space with a consistent set of parameters.

Surface diffuse scattering in XRR scans were taken into account by the use of a constant background whose value was determined from the intensity either side of the specular peak at high k_{1z}. Both dark noise and scattering from the bulk sample were found negligible in XRR and rocking scans.

Results

1. X-ray Reflectometry Measurements. By adopting the electron density commonly used for PS ($\rho_{\mathrm{PS}} = 0.324$ Å$^{-3\ 32}$) and hypothesizing a same electron density for amorphous PVC and CPB ($\rho_{\mathrm{CPB}} \approx \rho_{\mathrm{PVC}} = 0.429$ Å$^{-3\ 32}$), one must acknowledge that the contrast between the two homopolymers is small ($\Delta\rho_{\mathrm{CPB/PS}} = 0.115$ Å^{-3}) compared to the ones existing between Si/SiO$_x$ and CPB ($\Delta\rho_{\mathrm{Si/CPB}} = 0.267$ Å^{-3}) or between PS and air ($\Delta\rho_{\mathrm{PS/air}} = 0.324$ Å^{-3}). Reflectivity patterns being mostly sensitive to squared electron density gradients,[32] contributions from the substrate and air interfaces will tend to dominate the XRR data of our bilayers. It is thus very important to characterize as fully as possible the shapes of these interfaces on the single film samples beforehand. Contribution from the air interface was minimized by depositing onto CPB a PS layer being sufficiently thick to avoid Kiessig fringes arising from interferences at the air interface and sufficiently rough to minimize electron density gradients.

CPB onto Si/SiO$_x$. A representative profile of log(reflectivity × k_{1z}^4) vs k_{1z} for a CPB film deposited onto Si/SiO$_x$ subsequently used for the formation of bilayers is shown in Figure 1. Thanks to appropriate polymer concentration (1% w/v) and rotation speed (4000 rpm), CPB films with total thickness ($d_{\mathrm{CPB}} \approx 255$ Å) giving rise to well-defined Kiessig fringes are obtained. Joining the minima of the latter clearly reveals the presence of a low-amplitude/low-frequency modulation of the fringes whose period Δk_{1z} is around 0.13 Å^{-1}. This modulation corresponds to peaks in the derivative of the electron density profile separated by $\pi/\Delta k_{1z} \approx 24$ Å.

These observations on the raw data are consistent with the electron density profile (inset of Figure 1) derived from the a priori model-independent delumping procedure described in the Experimental Section. The presence of a dip of electron density at the substrate interface has already been observed for other homopolymers having relatively weak affinities to silicon oxide.[53] Its width (~26 Å) corresponds to the low-frequency modulation mentioned above, which rules out the dip being an artifact arising from the data analysis procedure. Additional proofs on the existence and discussion on the origin of these density perturbations at substrate surface may be found in ref 53.

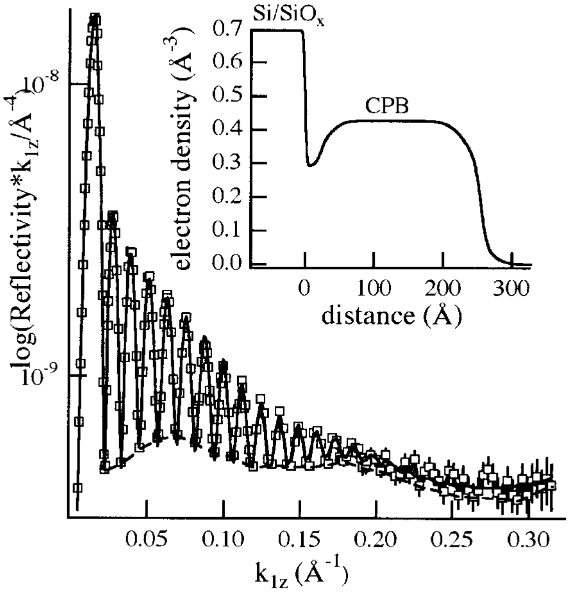

Figure 1. Reflectivity profile for a CPB film spin-coated onto a silicon wafer. Solid line is best fit calculated with the electron density profiles shown in the inset.

PS onto Float Glass. PS was spun-coated onto glass by choosing for the polymer concentration and rotation speed, values (3% w/v and 2000 rpm, respectively) that allow to generate films having a thickness d_{PS} of ca. 1360 Å and rms roughness σ_{PS} of ca. 17.5 Å. This thickness is such that Kiessig fringes due to interferences at the air interface cannot be resolved for bilayers but well in the single layer samples. The XRR scans of the bilayers thus only show oscillations due to interferences at the CPB/PS interface (see below), which simplifies considerably the interpretation.

Bilayers. Experimental XRR data for the bilayer sample are given in Figure 2. Results are shown before and after annealing for increasing times (2, 6, and 24 h) at 150 °C. The distance between the minima of the Kiessig fringes appearing for the unannealed bilayer ($\Delta k_{1z} \approx 0.12$ Å^{-1}) corresponds to the total thickness of the CPB layer determined above ($d_{\mathrm{CPB}} \approx 255$ Å). Interferences at the free surface which should have given rise to fringes with minima separated by $\pi/(d_{\mathrm{CPB}} + d_{\mathrm{PS}}) \approx 0.0019$ Å^{-1} and $\pi/d_{\mathrm{PS}} \approx 0.0023$ Å^{-1} are not observed, due to insufficient k_{1z} resolution and/or too small electron density gradients at the air interface.

Annealing the bilayer for 2 h at 150 °C (Figure 2, line B) induces (a) an increase of the separation distance between the Kiessig fringes related to the CPB layer which means a decrease of the thickness of the latter, (b) a more rapid damping of these fringes with k_{1z}, and (c) an increase of the amplitude of a low-frequency modulation which was hardly observable before annealing. The separation distance between minima of this oscillation ($\Delta k_{1z} \approx 0.125$ Å^{-1}) corresponds in direct space to electron density gradients ca. 25 Å apart. With longer annealing times (Figure 2, line B–D), the damping of the Kiessig fringes increases further, whereas the CPB layer thickness and the amplitude of the low-frequency modulation remain approximately constant.

These qualitative observations can be sharpened by the calculation of the electron density profiles giving

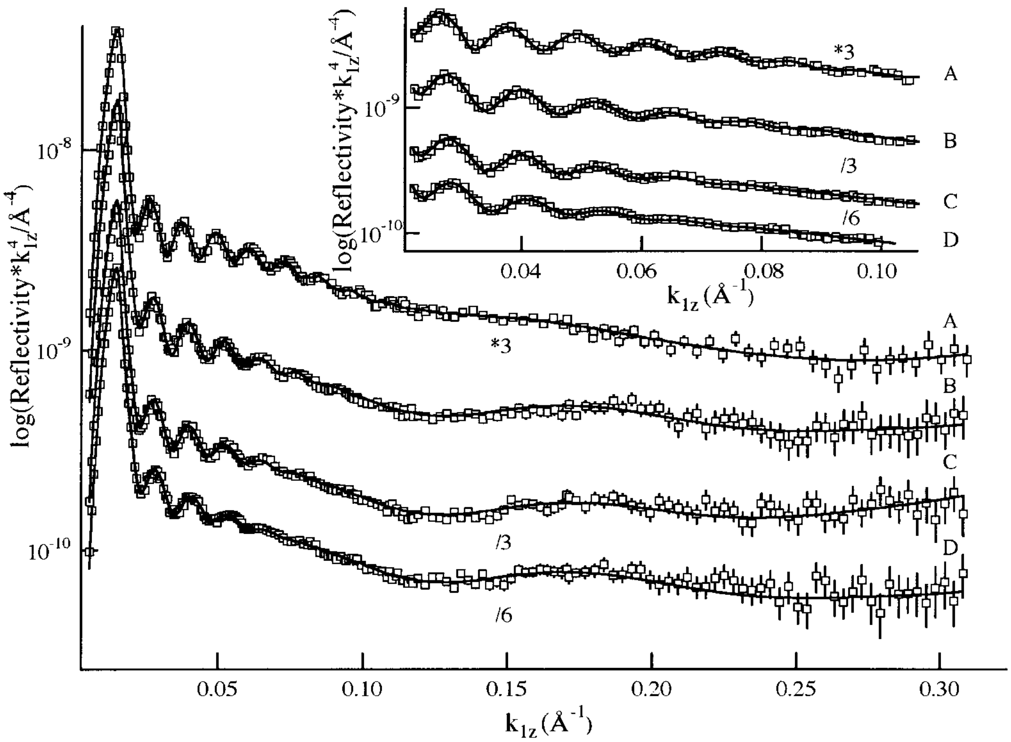

Figure 2. Reflectivity profiles for the CPB/PS bilayer systems: unannealed (line A), annealed for 2 h (line B); 6 h (line C); 24 h (line D). Solid lines are best fit calculated with electron density profiles shown in Figure 3.

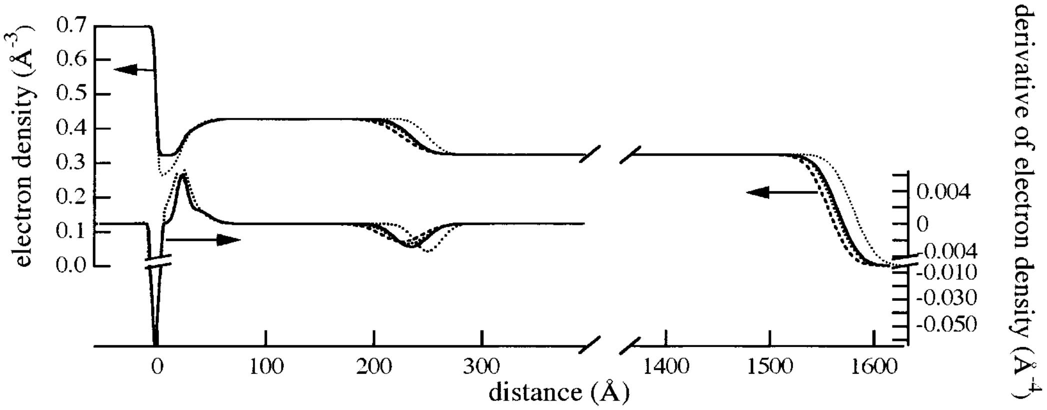

Figure 3. Electron density profiles derived from XRR data of Figure 2 (left). Unannealed bilayer (short dashes): annealed for 2 h (solid line); 6 h (dash–dotted line); 24 h (long dashes). Derivatives of the electron density near the substrate surface (right, same notation).

reflectivities in best agreement with the experimental data. To avoid nonuniqueness problems in data analysis, the profiles were derived using as much as possible a priori information provided by the continuous models derived for the corresponding single layer samples. The electron density profile at the interface between the two homopolymers is described by an error function with variance σ_m. Electron densities of the substrate (0.696 Å^{-3}) and of the homogeneous CPB (0.429 Å^{-3}) and PS (0.324 Å^{-3}) regions can be considered invariant during annealing (see above) and are fixed during all model optimizations. So is the roughness of the free surface; it is taken from the corresponding PS single layer sample (σ_{PS} = 17.5 Å). This assumption of unchanged roughness for the PS/air interface is supported by XRR experiments on PS films on glass or Si/SiO$_x$ annealed at 150 °C for comparable times; no significant change (within ±1 Å) in the surface roughness of the film could be detected. Calculated reflectivities not being sensitive to the PS layer thickness, this parameter is taken as the thickness of the PS single layer sample and kept constant for all fits.

The optimized electron density profiles are shown in Figure 3 along with their derivative against distance. The thinning of the CPB layer mentioned above can be quantified by following in function of the annealing time the separation distance between peaks in the electron density derivative profiles arising from gradients at the substrate and CPB/PS interfaces.

Two regimes clearly appear in the evolutions shown in Figure 4. At low annealing times (<2 h), one observes a rapid decrease of the thickness which is concomitant with a densification of the region with free volume excess near the solid substrate (Figure 3). The densification of this ca. 25 Å wide density dip results in a sharpening of its interface with the CPB film, while gradients at the substrate interface remain unchanged. This explains the amplitude enhancement of the oscil-

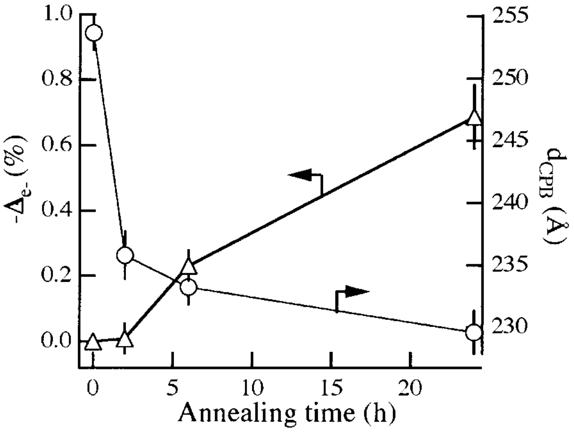

Figure 4. Variation upon annealing of the number of scatterers per sample unit surface (triangles) and CPB layer thickness (circles) as a function of annealing time at 150 °C.

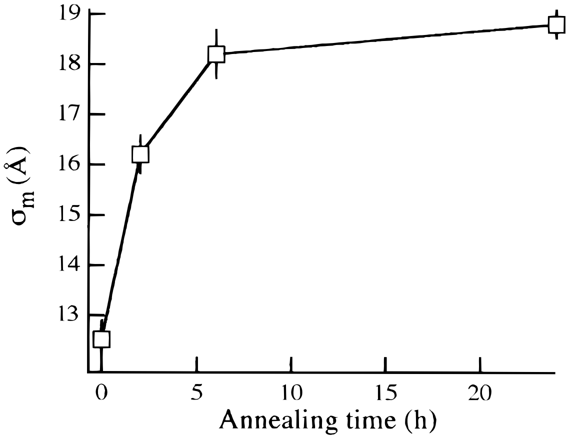

Figure 5. PS/CPB interfacial width as a function of annealing time at 150 °C as deduced from reflectivity scans.

lation of period $\Delta k_{1z} \approx \pi/25 = 0.125$ Å^{-1} observed in the XRR data after annealing (Figure 2).

The variation upon annealing of the total number of scattering electrons per unit sample surface has also been calculated:

$$\Delta_{e^-}(t) = \int_{-3\sigma_s}^{d_{tot}+3\sigma_f} (\rho_t(z) - \rho_0(z))\, dz \Big/ \int_{-3\sigma_s}^{d_{tot}+3\sigma_f} \rho_0(z)\, dz \quad (17)$$

where $\rho_0(z)$, $\rho_t(z)$, σ_s, σ_f, and d_{tot} are respectively the electron density profile before and after annealing at time t, the rms roughnesses of the substrate and of the free surface, and the total bilayer thickness. As the number of scattering units is approximately constant for 2 h annealing time (Figure 4), one can conclude that the thinning observed within this period is mainly governed by a reorganization of the polymer within the CPB layer. By contrast, for longer annealing times (>2 h), the shape of the density dip near the substrate does not change (Figure 3), the relaxation of the CPB in this region being probably complete. This is reflected in the XRR data by the steady amplitude of the low-frequency oscillation after 2 h annealing (Figure 2). However, a small thinning rate (Figure 4) is still observed which, with the slight but significant concomitant decrease (<1%) of the number of scattering units (Figure 4), suggests that, at these times, some slight HCl release from the CPB layer occurs. Significant dehydrochlorination of bulk CPB samples in a vacuum has been reported to begin at 190 °C.[54] However, this threshold temperature is highly dependent on the sample form.[54] The larger the sample specific area, the lower the threshold temperature. The observed dehydrochlorination does not however occur to a sufficient extent to lead to an observable decrease of the electron density.[49]

The last and most interesting structural change induced by the thermal treatment is the broadening of the CPB/PS interface. The decreasing contrast simply manifests itself in the experimental data through the increasing damping of the Kiessig fringes due to the CPB layer. The evolution of the measured interfacial width σ_m as a function of annealing time is shown in Figure 5. The width measured before annealing, $\sigma_m(0$ h$) = \sigma_0 = 12.5 \pm 0.4$ Å, is induced by sample preparation. After varying annealing times, σ_m increases and levels off after 10−12 h annealing time to a plateau value $\sigma_m(24$ h$) = 18.8 \pm 0.3$ Å. At this time, the system can be considered at equilibrium.

2. XDS Measurements. To investigate further the origin of the interfacial thickening observed in Figure 5, reflectivity scans were supplemented by rocking curves. Figure 6 gives the scattered intensity $\tilde{N}$ normalized against the incident intensity at specular position $\tilde{N}_{0,spec}$ recorded for $k_{1z} = 0.0285$ Å^{-1}, $k_{1z} = 0.0427$ Å^{-1}, and $k_{1z} = 0.0711$ Å^{-1}. Typical scans for the bilayer system before and after annealing for 2 and 24 h at 150 °C are shown. Annealing the system for 2 h leads to significant changes in the low k_{1z} scans; the diffuse scattering clearly decreases near the critical angle and slightly increases around the specular peak. Longer annealing times (e.g., 24 h in Figure 6) do not lead to further changes.

Before performing any fit, calculations were made to assess how sensitive are the calculated curves to the different parameters. Whereas significantly different results are obtained when the in-plane correlation lengths and roughness parameters of the CPB/PS and air interfaces ($\xi_{CPB/PS}$, ξ_{PS}, $H_{CPB/PS}$, and H_{PS}, respectively) are changed, one observes variations always far smaller than the error bars when the corresponding parameters for the substrate ($\xi_{Si/CPB}$, $H_{Si/CPB}$) are set to extreme values. $\xi_{Si/CPB}$ and $H_{Si/CPB}$ were thus set to reasonable but arbitrary values, and $\xi_{CPB/PS}$, ξ_{PS}, $H_{CPB/PS}$, and H_{PS} were the only fitting parameters.

XDS before Annealing. The rocking curves measured before annealing were analyzed using eqs 5, 6, 9, and 15. Thicknesses d_i, electron densities ρ_i, and rms roughnesses σ_i were taken from the XRR model shown in Figure 3 (short dashes) and kept constant during the fit. The electron density dip near the substrate was taken into account by a slice model with ca. 20 virtual layers being perfectly smooth ($\sigma_i = 0$ Å) on a rough substrate. This effectively assumes that the dip is due to free volume perturbations induced by the substrate that should be laterally uniform.[53] The thickness of the virtual layers (ca. 5 Å) was chosen sufficiently smaller than both the typical size of the gradient profile and the minimum dimension that can be discriminated in direct space ($\pi/(k_{1z})_{max} \approx 10$ Å). The effect of these layers on the incoherent intensity is minor; they only slightly affect the fields incident on and reflected from the substrate. The best fit is shown in Figure 7, and best parameters are collected in Table 1.

XDS after Annealing. To analyze the rocking curves after annealing, we again started from models derived from XRR experiments (Figure 3) and replaced the density dip by smooth virtual layers. We also assigned

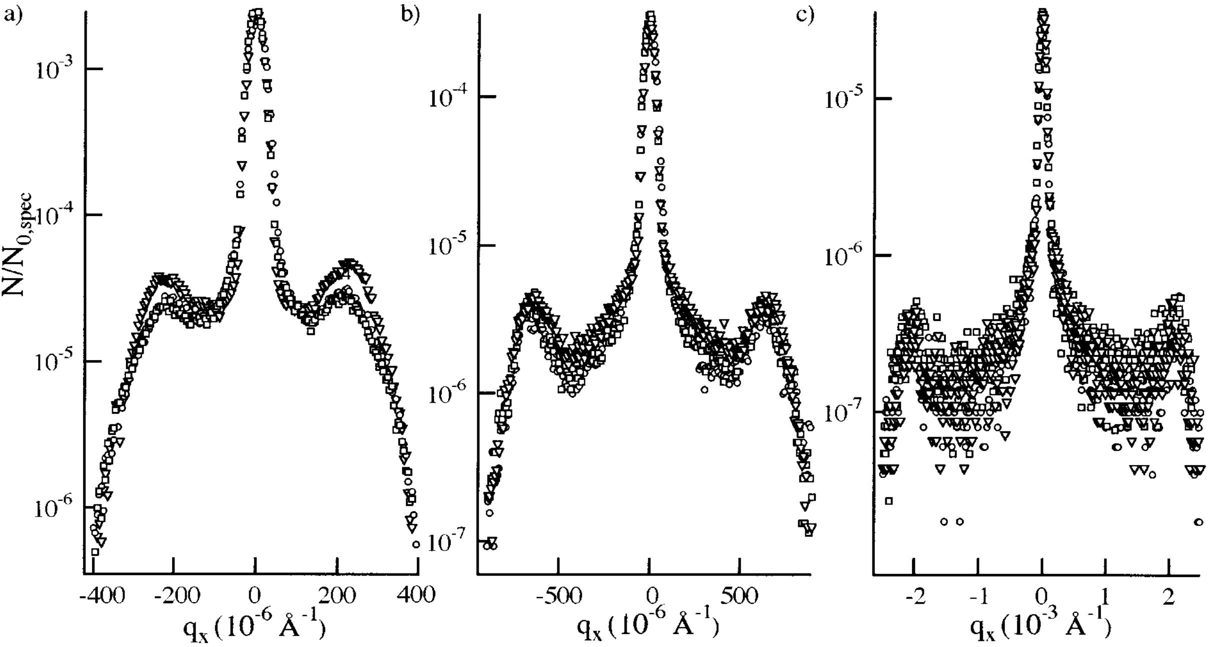

Figure 6. Rocking curves around $k_{1z} = 0.0285$ Å^{-1} (a), $k_{1z} = 0.0427$ Å^{-1} (b), and $k_{1z} = 0.0711$ Å^{-1} (c) for the bilayer before (open triangles) and after annealing (open circles, 2 h; open squares, 24 h).

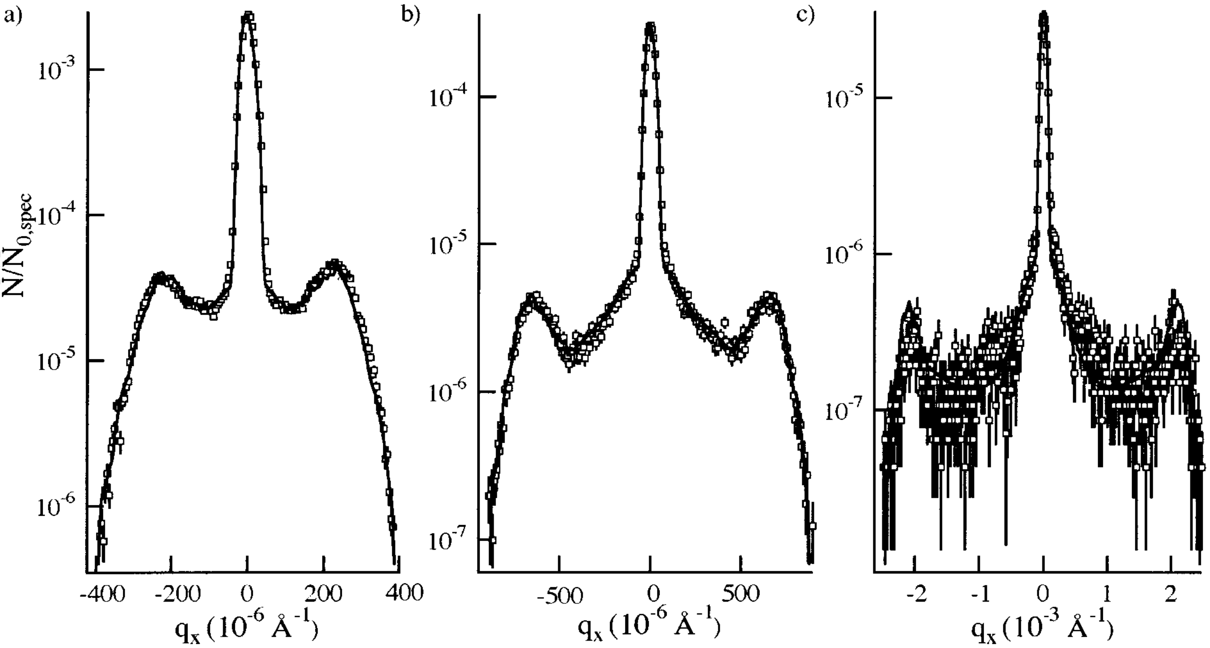

Figure 7. Rocking curves around $k_{1z} = 0.0285$ Å^{-1} (a), $k_{1z} = 0.0427$ Å^{-1} (b), and $k_{1z} = 0.0711$ Å^{-1} (c) for the bilayer before annealing (open squares). Solid lines are best fits to the experimental results. For parameters, see Table 1.

reasonable but arbitrary $\xi_{Si/CPB}$ and $H_{Si/CPB}$ to the substrate and ξ_{PS} and H_{PS} to the free surface. The two latter parameters were always adjusted to avoid any preassumption on the evolution of the free surface lateral roughness upon annealing. As expected, the observed densification of the dip after annealing (Figure 3) makes negligible difference in calculated rocking curves. The CPB/PS interface where interdiffusion takes place was replaced by 20 virtual layers of equal thickness with self-affine roughness profile having the same rms roughness σ_r, correlation length $\xi_{CPB/PS}$, and roughness parameter $H_{CPB/PS}$. The density of each virtual layer was fixed by error functions with variance given by the intrinsic width $\sigma_{CPB/PS} = \sqrt{\sigma_m^2 - \sigma_r^2}$. In the following, only fits to data measured after 24 h annealing are performed.

Three models were tested with respect to the modelization of the interdiffused interface:

1. First, fits to experimental data were performed considering that interdiffusion occurs without any change of the roughness profile due to sample preparation (eq 3). As shown in Figure 8 (left), this may be depicted by virtual layers having perfectly conformal roughness profiles with rms roughness $\sigma_r = \sigma_0$, correlation length $\xi_{CPB/PS}$, and roughness parameter $H_{CPB/PS}$ identical to those found before annealing (Table 1). ξ_{PS} and H_{PS} are thus the only adjustable parameters during a fit. Best fits to data (solid lines on the bottom curves of Figure

Table 1. XDS Fit Results

	before annealing	after annealing		
		eq 3	“correlated model”	“uncorrelated model”
σ_r (Å)[a]	12.5 ± 0.4	12.5 ± 0.4	17.1 ± 0.2	3.4 ± 0.2
$\sigma_{CPB/PS}$ (Å)[b]	0	14.0 ± 0.8	7.8 ± 1.2	18.5 ± 0.3
$\xi_{CPB/PS}$ (Å)[c]	9723 ± 625	9723 ± 625	19836 ± 912	29658 ± 1310
$H_{CPB/PS}$[d]	0.98 ± 0.02	0.98 ± 0.02	0.96 ± 0.04	0.73 ± 0.05
ξ_{PS} (Å)[e]	3052 ± 162	1025 ± 124	1095 ± 161	5850 ± 232
H_{PS}[f]	0.26 ± 0.03	0.22 ± 0.02	0.21 ± 0.02	0.2 ± 0.02

[a] Interfacial roughness from the XDS fit. [b] $\sigma_{CPB/PS} = \sqrt{\sigma_m^2(24h) - \sigma_r^2}$. [c] Lateral correlation length of the roughness profile at the CPB/PS interface. [d] Hurst exponent of the roughness profile at the CPB/PS interface. [e] Lateral correlation length of the roughness profile at the PS/air interface. [f] Hurst exponent of the roughness profile at the PS/air interface.

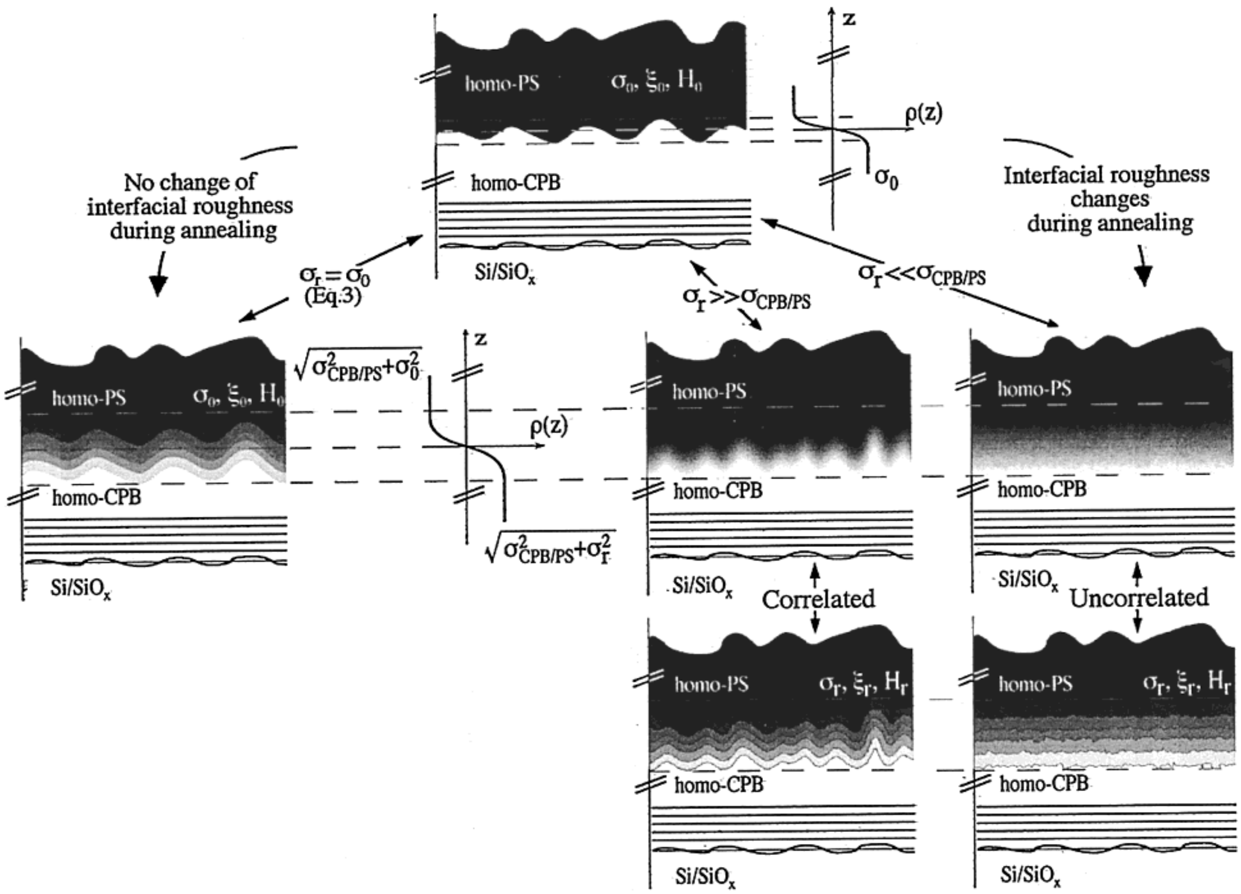

Figure 8. Sketch of the three different models used to interpret the XDS data. First, we assumed that interfacial roughness does not change during annealing ($\sigma_r = \sigma_0$, left). This hypothesis does not allow to fit properly the experimental data. Then we assumed that the spectrum of interfacial roughness changes during annealing (right). Two possible solutions were found from the data. The first one corresponds to the interfacial roughness being larger than the broadening due to interdiffusion only ($\sigma_r > \sigma_{CPB/PS}$; “correlated model”); the second one corresponds to the reverse ($\sigma_r \ll \sigma_{CPB/PS}$; “uncorrelated model”). The former solution is nearer to predictions from theory of capillary fluctuations.

9) were obtained adopting for the diffuse scattering cross section of the interdiffused interface expressions calculated in ref 49. While the drop of scattering near the critical angle can be properly reproduced with the best (ξ_{PS}, H_{PS}) pair, the scattering around the specular peak is largely underestimated. Hence, we may not consider eq 3 as a realistic approximation for describing our XDS data. In other words, the assumption that the initial roughness between CPB and PS is conserved during annealing is not correct.

2. Far better agreement can be obtained if one considers that the roughness profile at the CPB/PS interface evolves during annealing. In this case, besides ξ_{PS} and H_{PS}, σ_r, $\xi_{CPB/PS}$, and $H_{CPB/PS}$ must be adjusted. Two models giving equally satisfactory agreement to experiment can be found:

2.1. In the first one, the interfacial width determined by XRR originates dominantly from interfacial roughness; i.e., interdiffusion is restricted ($\sigma_r > \sigma_{CPB/PS}$). As shown in Figure 8, the interdiffused interface can then be modeled by virtual layers with perfectly conformal roughness profiles (“correlated model”). The density gradient is indeed sufficiently high for the slabs to keep a same roughness profile across the whole interface. Best fits within this model appearing in Figure 9 (solid lines on middle curves) have been achieved using for the differential cross section the same expressions as for the eq 3 approximation (Table 1, “correlated model”).

2.2. Figure 9 (solid lines on the upper curves) shows that equally satisfactory fits can be obtained with a model where interdiffusion is predominant ($\sigma_r \ll \sigma_{CPB/PS}$). In this case (Figure 8), density gradients are so small

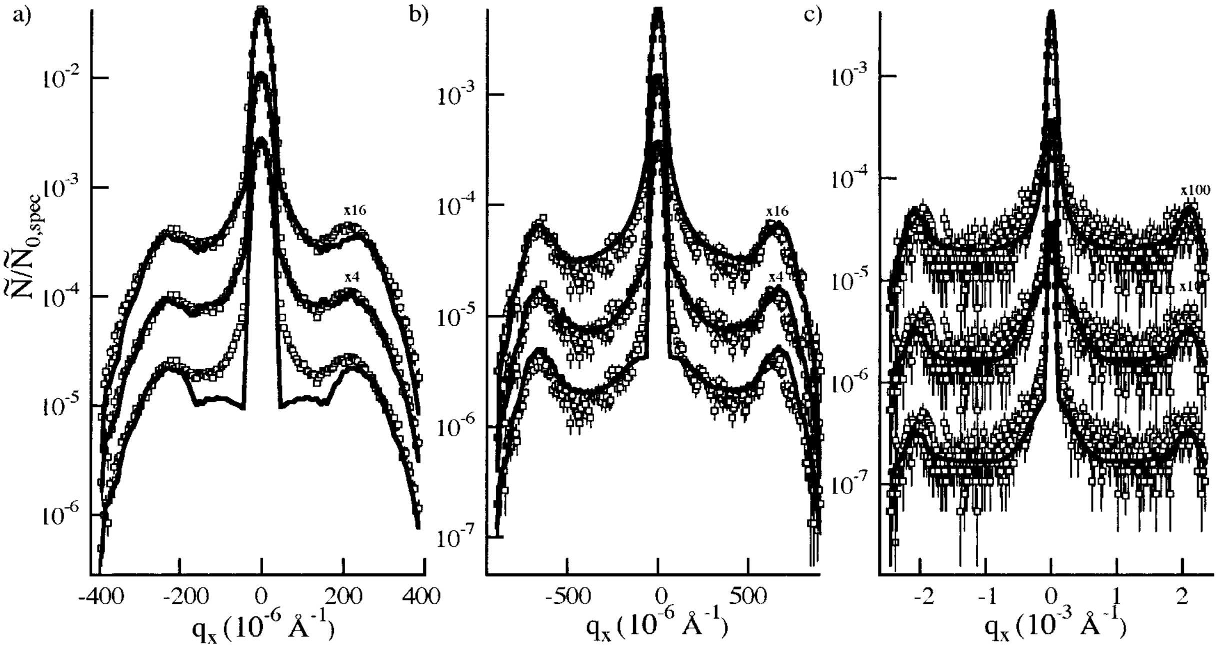

Figure 9. Rocking curves around $k_{1z} = 0.0285$ Å^{-1}(a), $k_{1z} = 0.0427$ Å^{-1} (b), and $k_{1z} = 0.0711$ Å^{-1} (c) for the bilayer after annealing. Solid lines are best fits using, from bottom to top, eq 3, eq 4 with a correlated model, and eq 4 with an uncorrelated model, respectively.

that a given roughness profile cannot propagate itself very far across the interface. This situation can be depicted by rough interfacial slabs having uncorrelated roughness profiles ("uncorrelated model"). Best fits are calculated with parameters of Table 1 using for the diffuse scattering cross section expressions for multilayers with interfaces having uncorrelated interfacial roughnesses.[33]

Discussion

The previous analysis allows to reject unambiguously the hypothesis that the initial roughness due to sample preparation does not vary during annealing. However, when we consider roughness variation at the CPB/PS interface during annealing, the XDS data after annealing can be analyzed using two models displaying very different amplitudes for the roughness at the CPB/PS interface. It is thus interesting to compare the experimental results to predictions from existing theories calculating the broadening of interfaces separating two media A and B by capillary waves. Equation 12 can be rewritten as

$$\sigma_{\mathrm{fl}}^2 \cong \frac{kT}{2\pi\gamma}\ln\left(\frac{q_{\mathrm{U}}}{q_{\mathrm{L}}}\right) = \frac{kT}{2\pi\gamma}\ln\left(\frac{\sqrt{\gamma/K}}{\sqrt{\dfrac{\Delta\rho g + \alpha}{\gamma} + \left(\dfrac{2\pi}{L_{\mathrm{cx}}}\right)^2}}\right) \qquad (18)$$

For our bilayer system, $4\pi^2/L_{\mathrm{cx}}^2$ may be estimated in our XRR experiments to increase from 0.07 μm^{-2} at $k_{1z} = (k_c)_{\mathrm{Si/SiO_x}}$ up to 27.4 μm^{-2} at $k_{1z} = (k_{1z})_{\mathrm{max}} = 0.32$ Å^{-1}.[49] Estimating $\gamma = 3 \times 10^{-3}$ J/m^2, a typical value for most polymer/polymer interfaces,[55] $\rho_{\mathrm{PS}}^{\mathrm{m}} = 1.04$ g/cm^3 [32] and $\rho_{\mathrm{CPB}}^{\mathrm{m}} \approx \rho_{\mathrm{PVC}}^{\mathrm{m}} = 1.358$ g/cm^3,[32] we find that the gravitational term ($\Delta\rho g/\gamma$) is several orders smaller than the coherence length term and can thus be neglected.

For our system, the van der Waals term (α/γ) in eq 18 can be computed from the Hamaker constant for the interaction between air and CPB through the PS film ($A_{\mathrm{CPB/PS/air}}$) and from the Hamaker constant for the interaction between the (Si/SiO$_2$) substrate and PS through the CPB film ($A_{\mathrm{(Si/SiO_2)/CPB/PS}}$), using

$$\alpha = \frac{A_{\mathrm{CPB/PS/air}}}{2\pi D_{\mathrm{PS}}^4} + \frac{A_{\mathrm{(Si/SiO_2)/CPB/PS}}}{2\pi D_{\mathrm{CPB}}^4} \qquad (19)$$

where D_{PS} and D_{CPB} are the thickness of the PS and CPB films, respectively. We have estimated Hamaker constants on the basis of the Lifshitz theory.[49,56,57] We obtain for the Hamaker constant between CPB and air through the 1385 Å thick PS layer a very small value at 150 °C, $A_{\mathrm{CPB/PS/air}}$(1385 Å, 150 °C) = 1.86×10^{-22} J. The corresponding value for α/γ is 2.68×10^{-5} μm^{-2}, with γ estimated as 3×10^{-3} J/m^2, which is again much smaller than the coherence length term. We can thus safely conclude that van der Waals forces existing between CPB and air across the thick PS layer do not affect the capillary wave spectrum at the CPB/PS interface. This is in contrast with the effect of the dispersion forces existing between the silicon substrate and the PS layer through the 230 Å thick CPB layer. The substrate may be approximated as a semiinfinite Si medium coated with a thin amorphous SiO$_2$ layer with a typical thickness $d_{\mathrm{SiO_2}}$ lying between 10 and 20 Å.[48] Applying the Lifshitz theory for this geometry,[49,57] the Hamaker constant $A_{\mathrm{(Si/SiO_2)/CPB/PS}}$(230 Å, 150 °C) between the Si/SiO$_2$ substrate and the PS layer is found to vary slightly from 1.95×10^{-21} J when $d_{\mathrm{SiO_2}} = 10$ Å down to 1.74×10^{-21} J when $d_{\mathrm{SiO_2}} = 20$ Å. The corresponding value estimated for α/γ is 0.33−0.37 μm^{-2}, which is of the same order as the coherence length term and may thus not be neglected.

Knowing the Hamaker constants, the amplitude of the fluctuations at the CPB/PS interface (σ_{fl}) can be deduced from eqs 1, 2, 4, and 18, provided a suitable expression is adopted for the interfacial energy. Mean-field theories for incompressible blends in the strong segregation limit lead to

Table 2. Comparison between Different Approaches

	theory of fluctuations		fits to the XDS data		other approaches	
	$L_{cx}((k_c)_{Si/SiO_x})$	$L_{cx}(0.32\ Å^{-1})$	"correlated model"	"uncorrelated model"	heat of mixing	solubility parameters
σ_r (Å)[a]	14.6 ± 0.6	13.0 ± 0.6	17.1 ± 0.2	3.4 ± 0.2		
$\sigma_{CPB/PS}$ (Å)[b]	11.9 ± 1.4	13.5 ± 1.2	7.8 ± 1.2	18.5 ± 0.3	(22)[c]	9[c]
$\chi_{CPB/PS}$	0.046 ± 0.003	0.036 ± 0.002	0.113 ± 0.033	0.023 ± 0.001	0.017	0.077

[a] Rms roughness of the CPB/PS interface. [b] Rms width of the interdiffused boundary at the CPB/PS interface. [c] Computed from the value of $\chi_{CPB/PS}$ using eqs 1 and 2.

$$\gamma_{AB} = \gamma_{AB}^{\infty}\left(1 - L'\left(\frac{1}{\chi_{AB}P_A} + \frac{1}{\chi_{AB}P_B}\right)\right) \qquad (20)$$

where

$$\gamma_{AB}^{\infty} = \frac{2}{3}\frac{k_BT}{\sqrt{6}}\frac{\chi_{AB}^{1/2}}{(v_Av_B)^{1/4}}\left(\frac{(b_A/v_A)^3v_A^{3/2} - (b_B/v_B)^3v_B^{3/2}}{(b_A/v_A)^2v_A - (b_B/v_B)^2v_B}\right) \qquad (21)$$

and L' is equal to either $\pi^2/12$ (Broseta's work[27]) or 1.35 (Tang–Freed's theory[28]). Hence, σ_{fl} can be written as a function of σ_m, b_A, b_B, v_A, v_B, P_A, P_B, T, $A_{(Si/SiO_2)/CPB/PS}$, and L_{cx}. The first two columns of Table 2 show the results using σ_m(24 h) found by XRR after 24 h and for L_{cx} set to its extreme values calculated at $k_{1z} = (k_c)_{Si/SiO_x}$ and $k_{1z} = 0.32$ Å^{-1}, respectively. The corresponding $\sigma_{CPB/PS} = \sqrt{\sigma_m^2(24h) - \sigma_{fl}^2}$ values are also shown. The statistical segment lengths ($b_{CPB} \approx b_{PVC} = 7.2$ Å,[59] $b_{PS} = 6.8$ Å[58]) and monomer specific volumes ($v_{CPB} \approx v_{PVC} = 75$ Å^3,[32] $v_{PS} = 165$ Å^3 [32]) are tabulated values. The degrees of polymerization ($2P_{CPB} = 538$[60] and $P_{PS} = 442$) were determined from SEC results (see Experimental Section) assuming that the polybutadiene is fully chlorinated. Note that differences between values calculated with L and L' are negligible within errors due to uncertainties in σ_m(24 h). Similarly, the calculated σ_{fl} are quite insensitive to the choice of thickness of the SiO_2 layer.

Considering the σ_{fl} and $\sigma_{CPB/PS}$ values, Table 2 shows that it is the correlated model which gives the closer agreement to capillary waves theory. Nevertheless, the agreement is far from being excellent, which may be due to a couple of reasons. First, we have considered the rms roughness of the outer interface of the PS film to be constant during annealing, which is only an approximation. Second, the spectrum of capillary waves may be affected by the dimensions of the system.[60] This, however, will not contribute to reduce the discrepancy between the theoretical prediction and our experimental findings. Third, we have used for the height–height correlation function the general form of eq 9, while a direct fit using eq 8 would have been more appropriate.

Once $\sigma_{CPB/PS}$ is known, $\chi_{CPB/PS}$ can be deduced from eqs 1 and 2 (Table 2). The only experimental χ value found in the literature that can be compared to the values gathered in Table 2 comes from calorimetric experiments on model compounds.[61] An interaction parameter value of 0.017 was obtained by measuring the endothermic heat arising when 1,3-dichlorobutane and styrene oligomers of increasing length[61] are mixed. This value is however not compatible with our results, since the width of the interdiffused region computed from $\chi_{CPB/PS} = 0.017$ is significantly larger than the total interfacial width (roughness included) measured by XRR.

Another comparison can be made with χ values determined from solubility parameters δ_i of both components A and B:

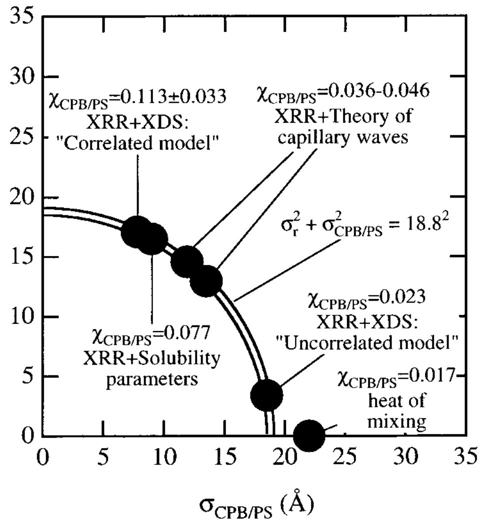

Figure 10. Summary of the different solutions found by various approaches. The vertical axis (σ_r) represents the contribution from interfacial roughness to the total interfacial width between PS and CPB, while the horizontal axis represents the contribution due to interdiffusion ($\sigma_{CPB/PS}$). Because the total interfacial width is known from XRR, the locus of possible solutions is restricted to a circle of radius 18.8 Å. The spots on the circle indicate values of ($\sigma_{CPB/PS}$, σ_r) found using different approaches (see text and Figure 8) and the associated values of interaction parameter $\chi_{CPB/PS}$. The predictions from theory of capillary waves are nearer to one of the possible solutions obtained from the fit of the XDS data ($\sigma_r > \sigma_{CPB/PS}$; "correlated model").

$$\chi_{AB} = \frac{v_A}{k_BT}(\delta_A - \delta_B)^2 \qquad (22)$$

where v_A is the specific monomer volume of the smallest species. In our system, CPB has the smaller specific monomer volume and, as above, we take $v_{CPB} \approx v_{PVC} = 75$ Å^3. Average experimental values for the solubility parameters taken from the literature[23] are $\delta_{CPB} \approx \delta_{PVC} = 20.7$ J$^{1/2}$ cm$^{-3/2}$ and $\delta_{PS} = 18.2$ J$^{1/2}$ cm$^{-3/2}$. Inserting these figures in eq 22 gives $\chi_{CPB/PS} = 0.077$. Acknowledging the large scattering on the published solubility parameters, this result can be considered as qualitative only. The value lies between the two $\chi_{CPB/PS}$ determined by XDS.

Figure 10 summarizes solutions found by various approaches. As can be noticed, the results found by the fit of the XDS data with the correlated model, the predictions from the theory of capillary waves, and the values obtained from solubility parameters lie close together on the circle of possible solutions in the roughness/interdiffusion plane. By contrast, the uncorrelated model provides quite different results, while the heat of mixing experiments do not even lead to thickness values compatible with the total interfacial width determined by XRR. This figure suggests strongly that capillary wave fluctuations are indeed the main source of interfacial broadening for CPB/PS blends. Because of this, small errors in the determination of interfacial roughness translate in large variations in the exact value of the interaction parameter (Figure 10).

Conclusions

Thanks to its angstrom resolution, XRR turned out to be a suitable technique for following the formation of the very thin interface between PS and CPB upon annealing at 150 °C.

For the first time, experimental attempts have been made to distinguish between the two contributions to the interfacial width measured by XRR: the width due to interdiffusion ($\sigma_{\mathrm{CPB/PS}}$) and the width due to roughness (σ_{r}). For this purpose, laterally averaged experiments were supplemented by off-specular (XDS) experiments sensitive to lateral correlations.

The analysis of the XDS data allowed us to unambiguously reject the assumption often made in the literature that neglects the evolution of the roughness profile at the polymer−polymer interface during annealing.

At least two very different models could equally satisfactorily describe the XRR and XDS data. XDS measurements are thus intrinsically not capable to help decide unambiguously whether the remaining roughness at the interdiffused interface stems only from a spectrum of capillary waves. Although differences exist between fit values and theoretical values derived from existing theories on thermal fluctuations, a comparison between results obtained by different approaches (Figure 10) suggests that capillary wave fluctuations are indeed the main source of interfacial broadening for CPB/PS blends.

Acknowledgment. The authors express their gratitude to Profs. R. Jérôme and P. Dubois for their help with the synthesis of the polybutadiene used in this study and to the National Fund for Scientific Research (Belgium) for partial financing of this work.

References and Notes

(1) Chujo, R. *Polym. J.* **1991**, *23*, 367.
(2) Composto, R. J.; Kramer, E. J.; White, D. M. *Macromolecules* **1988**, *21*, 2580.
(3) Kim, C. K.; Kramer, E. J.; Osby, J. O.; Walsh, D. J. *J. Polym. Sci. A* **1995**, *33*, 467.
(4) Kerle, T.; Klein, J.; Binder, K. *Phys. Rev. Lett.* **1996**, *77*, 1316.
(5) Endisch, D.; Rauch, F.; Götzelmann, A.; Reiter, G.; Stamm, M. *Nucl. Instrum. Methods B* **1992**, *33*, 467.
(6) Stamm, M.; Schubert, D. W. *Annu. Rev. Mater. Sci.* **1995**, *25*, 325.
(7) Fernandez, M. L.; Higgins, J. S.; Penfold, J.; Ward, R. C.; Stackelton, C.; Walsh, D. J. *Polymer* **1988**, *29*, 1923.
(8) Anastasiadis, S. H.; Russell, T. P.; Satija, S. K.; Majkrzak, C. F. *J. Chem. Phys.* **1990**, *92*, 5677.
(9) Sferazza, M.; Xiao, C.; Jones, R. A. L.; Bucknall, D. G.; Webster, J.; Penfold, J. *Phys. Rev. Lett.* **1997**, *78*, 3693.
(10) Siqueira, D.; Schubert, D. W.; Erb, V.; Stamm, M.; Amato, J. P. *Colloid Polym. Sci.* **1995**, *273*, 1041.
(11) Schubert, D. W.; Abetz, V.; Stamm, M.; Hack, T.; Siol, W. *Macromolecules* **1995**, *28*, 2519.
(12) Hermes, H. E.; Higgins, J. S.; Bucknall, D. G. *Polymer* **1997**, *38*, 985.
(13) Hüttenbach, S.; Stamm, M.; Reiter, G.; Foster, M. *Langmuir* **1991**, *7*, 2438.
(14) Helfand, E.; Tagami, Y. *J. Chem. Phys.* **1971**, *56*, 3592.
(15) Helfand, E.; Sapse, A. M. *J. Chem. Phys.* **1975**, *62*, 1327.
(16) Shiomi, T.; Kohno, K.; Yoneda, K.; Tomita, T.; Miya, M.; Imai, K. *Macromolecules* **1985**, *18*, 414.
(17) El-Hibri, M. J.; Cheng, W.; Munk, P. *ACS Polym. Mater. Sci. Eng.* **1988**, *58*, 741.
(18) Nishi, T.; Wang, T. T. *Macromolecules* **1975**, *6*, 909.
(19) Uriarte, C.; Eguizabal, J. I.; Llanos, M.; Iribarren, J. I.; Iruin, J. J. *Macromolecules* **1987**, *20*, 3038.
(20) Fukuda, T.; Nagata, M.; Inagaki, H. *Macromolecules* **1985**, *17*, 548.
(21) Kim, C. K.; Paul, D. R. *Polymer* **1992**, *33*, 1630.
(22) Callaghan, T. A.; Paul, D. R. *Macromolecules* **1993**, *26*, 2439.
(23) Van Krevelen, D. W. *Properties of Polymers-Their Estimation and Correlation with Chemical Structure,* 3rd ed.; Elsevier: New York, 1990; p 200 ff.
(24) Roe, R. R.; Fishkis, M.; Chang, J. C. *Macromolecules* **1981**, *14*, 1091.
(25) Russell, T. P.; Hjelm, R. P.; Seegers, P. A. *Macromolecules* **1990**, *23*, 890.
(26) Zhou, X. L.; Chen, S. H. *Phys. Rev. Lett.* **1985**, *55*, 2425.
(27) Broseta, D.; Frederickson, G. H.; Helfand, E.; Leibler, L. *Macromolecules* **1990**, *23*, 132.
(28) Tang, H.; Freed, K. F. *J. Chem. Phys.* **1991**, *94*, 6307.
(29) Semenov, A. N. *Macromolecules* **1993**, *26*, 6617.
(30) Shull, K. R.; Mayes, A. N.; Russell, T. P. *Macromolecules* **1993**, *26*, 3929.
(31) Semenov, A. N. *Macromolecules* **1994**, *27*, 2732.
(32) Russell, T. P. *Mater. Sci. Rep.* **1990**, *5*, 186.
(33) Holy, V.; Kubena, J.; Ohlidal, I.; Lischka, K.; Plotz, W. *Phys. Rev. B* **1993**, *47*, 15896.
(34) Sinha, S. K. *J. Phys. III* **1994**, *4*, 1543.
(35) Holy, V.; Baumbach, T. *Phys. Rev. B* **1994**, *49*, 10668.
(36) Daillant, J.; Bosio, L.; Harzallah, B.; Benattar, J. J. *J. Phys. II* **1991**, *1*, 149.
(37) Meunier, J. *J. Phys. (Paris)* **1987**, *48*, 1819.
(38) Gourier, C.; Daillant, J.; Braslau, A.; Alba, M.; Quinn, K.; Luzet, D.; Blot, C.; Chatenay, D.; Grübel, G.; Legrand, J.-F.; Vignaud, G. *Phys. Rev. Lett.* **1997**, *78*, 3157.
(39) Israelachvili, J. N. *Intermolecular and Surface Forces*, 2nd ed.; Academic Press: London, 1992; p 176 ff.
(40) Tidswell, I. M.; Rabedeau, T. A.; Pershan, P. S.; Kosowsky, S. D. *Phys. Rev. Lett.* **1991**, *66*, 2108.
(41) Sinha, S. K.; Sirota, E. B.; Garoff, S.; Stanley, H. B. *Phys. Rev. B* **1988**, *38*, 2297.
(42) Buff, F. P.; Lovett, R. A.; Stillinger, F. H. *Phys. Rev. Lett.* **1965**, *15*, 621.
(43) Rowlinson, J. S.; Widom, B. *Molecular Theory of Capillarity*; Clarendon Press: Oxford, 1982.
(44) Braslau, A.; Deutsch, Pershan, P. S.; Weiss, A. H.; Als-Nielsen, J.; Bohr, J. *Phys. Rev. Lett.* **1985**, *54*, 114.
(45) Braslau, A.; Pershan, P. S.; Swislow, G.; Ocko, B. M.; Als-Nielsen, J. *Phys. Rev. A* **1988**, *38*, 2457.
(46) Totsmann, H.; DiMasi, E.; Pershan, P. S.; Ocko, B. M.; Shpyrko, O. G.; Deutsch, M. *Phys. Rev. B* **1999**, *59*, 783.
(47) Stone, V. W.; Jonas, A. M.; Legras, R.; Dubois, P.; Jérôme, R. *J. Polym. Sci., Polym. Chem. Ed.* **1999**, *37*, 233.
(48) Carim, A. H.; Dovek, M. M.; Quate, C. F.; Sinclair, R.; Vorst, C. *Science* **1987**, *237*, 630.
(49) Stone, V. W. PhD Thesis, UCL, 1999.
(50) Parrat, G. *Phys. Rev.* **1954**, *95*, 359.
(51) Pedersen, J. K.; Hamley, I. W. *J. Appl. Crystallogr.* **1994**, *27*, 36.
(52) De Boer, D. K. G. *Phys. Rev. B* **1996**, *53*, 6048.
(53) Bolline, C.; Stone, V. W.; Jonas, A. M. *Macromolecules* **1999**, *32*, 4719.
(54) Crawley, S.; McNeill, I. C. *J. Polym. Sci., Polym. Chem. Ed.* **1978**, *16*, 2593.
(55) Wu, S. *Polymer Interface and Adhesion*; Marcel Dekker: New York, 1982; p 108.
(56) Mahanty, J.; Ninham, B. *Dispersion Forces*; Academic Press: New York, 1976; p 143.
(57) Prieve, D. C.; Russel, W. B. *J. Colloid Interface Sci.* **1988**, *125*, 1.
(58) Sato, M.; Koshiishi, Y.; Asahina, M. *J. Polym. Sci., Part B: Polym. Lett. Ed.* **1963**, *1*, 233.
(59) We have taken for the degree of polymerization of the CPB segment or chain $2P_{\mathrm{CPB}}$ ($P_{\mathrm{CPB}} = \bar{M}_{\mathrm{n,CPB}}/125$) in order to be coherent with the choice of b_{CPB} and v_{CPB}.
(60) Kerle, T.; Klein, J.; Binder, K. *Phys. Rev. Lett.* **1996**, *77*, 1318.
(61) Kim, J. H.; Barlow, J. W.; Paul, D. R. *J. Polym. Sci. B* **1989**, *27*, 2211.

MA990306U